

# Investigation of Precipitation Process in the Water Vapor Channel of the Yarlung Zsangbo Grand Canyon

Xuelong Chen<sup>①</sup>, Xiangde Xu, Yaoming Ma, Gaili Wang, Deliang Chen, Dianbin Cao, Xin Xu, Qiang Zhang, Luhan Li, Yajing Liu, Liping Liu, Maoshan Li, Siqiong Luo, Xin Wang, and Xie Hu

**KEYWORDS:**

Mountain meteorology; Precipitation; In situ atmospheric observations; Atmosphere-land interaction; Valley/mountain flows; Water vapor

**ABSTRACT:** The Yarlung Zsangbo Grand Canyon (YGC) is an important pathway for water vapor transport from southern Asia to the Tibetan Plateau (TP). This area exhibits one of the highest frequencies of convective activity in China, and precipitation often induces natural disasters in local communities, which can dramatically affect their livelihoods. In addition, the produced precipitation gives rise to vast glaciers and large rivers around the YGC. In 2018, the Second Tibetan Plateau Scientific Expedition and Research Program tasked a research team to conduct an “investigation of the precipitation process in the water vapor channel of the Yarlung Zsangbo Grand Canyon” (INVC) in the southeastern TP. This team subsequently established a comprehensive observation system of land–air interaction, water vapor, clouds, and rainfall activity in the YGC. This paper introduces the developed observation system and summarizes the preliminary results obtained during the first two years of the project. Using this INVC observation network, herein, we focus on the development of rainfall events on the southeastern TP. This project also helps to monitor geohazards in the key area of the Sichuan–Tibet railway, which traverses the northern YGC. The observation datasets will benefit future research on mountain meteorology.

<https://doi.org/10.1175/BAMS-D-23-0120.1>

Corresponding authors: Xuelong Chen, [x.chen@itpcas.ac.cn](mailto:x.chen@itpcas.ac.cn); Yaoming Ma, [ymma@itpcas.ac.cn](mailto:ymma@itpcas.ac.cn)

Supplemental material: <https://doi.org/10.1175/BAMS-D-23-0120.2>

In final form 31 October 2023

© 2024 American Meteorological Society. This published article is licensed under the terms of the default AMS reuse license. For information regarding reuse of this content and general copyright information, consult the AMS Copyright Policy ([www.ametsoc.org/PUBSReuseLicenses](http://www.ametsoc.org/PUBSReuseLicenses)).

**AFFILIATIONS:** X. Chen, Ma, Cao, Xin Xu, Zhang, L. Li, and Y. Liu—Land-Atmosphere Interaction and Its Climatic Effects Group, State Key Laboratory of Tibetan Plateau Earth System, Environment and Resources (TPESER), Institute of Tibetan Plateau Research, Chinese Academy of Sciences, Beijing, China; Xiangde Xu, G. Wang, and L. Liu—State Key Laboratory of Disastrous Weather, China Academy of Meteorological Sciences, Beijing, China; D. Chen—Regional Climate Group, Department of Earth Science, University of Gothenburg, Gothenburg, Sweden; M. Li—College of Atmospheric Sciences, Plateau Atmosphere and Environment Key Laboratory of Sichuan Province, Chengdu University of Information Technology, Chengdu, China; Luo and X. Wang—Key Laboratory of Land Surface Process and Climate Change in Cold and Arid Regions, Northwest Institute of Eco-Environment and Resources, Chinese Academy of Sciences, Lanzhou, China; Hu—College of Urban and Environmental Sciences, Peking University, Beijing, China

The Tibetan Plateau (TP) is often referred to as the “water tower” of Asia (Xu et al. 2008). Due to the heating of the plateau (Wu and Zhang 1999) in the summer, strong low-level convergence of the atmospheric flow occurs over the plateau, creating conditions that allow water vapor to be transported from the ocean to the plateau (Xu et al. 2008). When warm and humid ocean air reaches the plateau, some of the water vapor ascends along the southern slope of the plateau, resulting in frequent convective events (Xu et al. 2008). The topographic barrier created by the Himalaya Mountains makes it difficult for water vapor from the south to directly enter the hinterland of the plateau (Boos and Kuang 2010), except by traversing the meridional canyons in the Himalayas (Lin et al. 2018). The Yarlung Zsangbo Grand Canyon (YGC) is one of the largest canyons in the world (Fig. 1), and it acts as a major pathway for water vapor transport from the Indian mainland to the TP (Gao 2012; Yuan et al. 2022). Glacier retreat has significantly accelerated in the YGC region during the past 30 years (Yao et al. 2012). The glaciers around the YGC are deeply influenced by the precipitation caused by the South Asian monsoon system (Yang et al. 2010). The disappearance of glaciers has been accompanied by a decrease in precipitation in this area. The YGC is one of the regions on the TP with the greatest decreases in snowfall and rainfall (Chen et al. 2024). The meridional water vapor transported to the YGC by the South Asian monsoon has continuously declined (Chen et al. 2024). Correlation analysis between the precipitation on the TP and the water vapor transport through the YGC entrance region has demonstrated that the precipitation on the southeastern TP (SEP) is closely related to the meridional water vapor transport through the YGC (Chen et al. 2024). In addition, the numerical simulation conducted by Yuan et al. (2022) also demonstrated that the moisture transport through this channel is critical to precipitation in the YGC region. Meanwhile, the lack of observations in the YGC makes it difficult to verify precipitation modeling in this region, which hinders numerical weather prediction. Thus, it is critical to observe the water vapor and cloud precipitation processes in the YGC.

The YGC exhibits the highest frequency of convective activity in the form of extreme rainfall compared to other regions on the TP (Jian et al. 2012; Kukulies et al. 2020). Due to frequent rainstorms in the wet season, natural disasters such as landslides and debris flows frequently occur, and often block traffic corridors. The analysis of precipitation mechanisms within the YGC is also of great significance for national park construction within the YGC (Xu 2019). Thus, understanding the relationship between water vapor changes, convective cloud activity, and extreme rainfall events in the YGC is critical. Unfortunately, previous observation experiments over the plateau were mainly focused on flat (low-relief) surfaces or in the middle

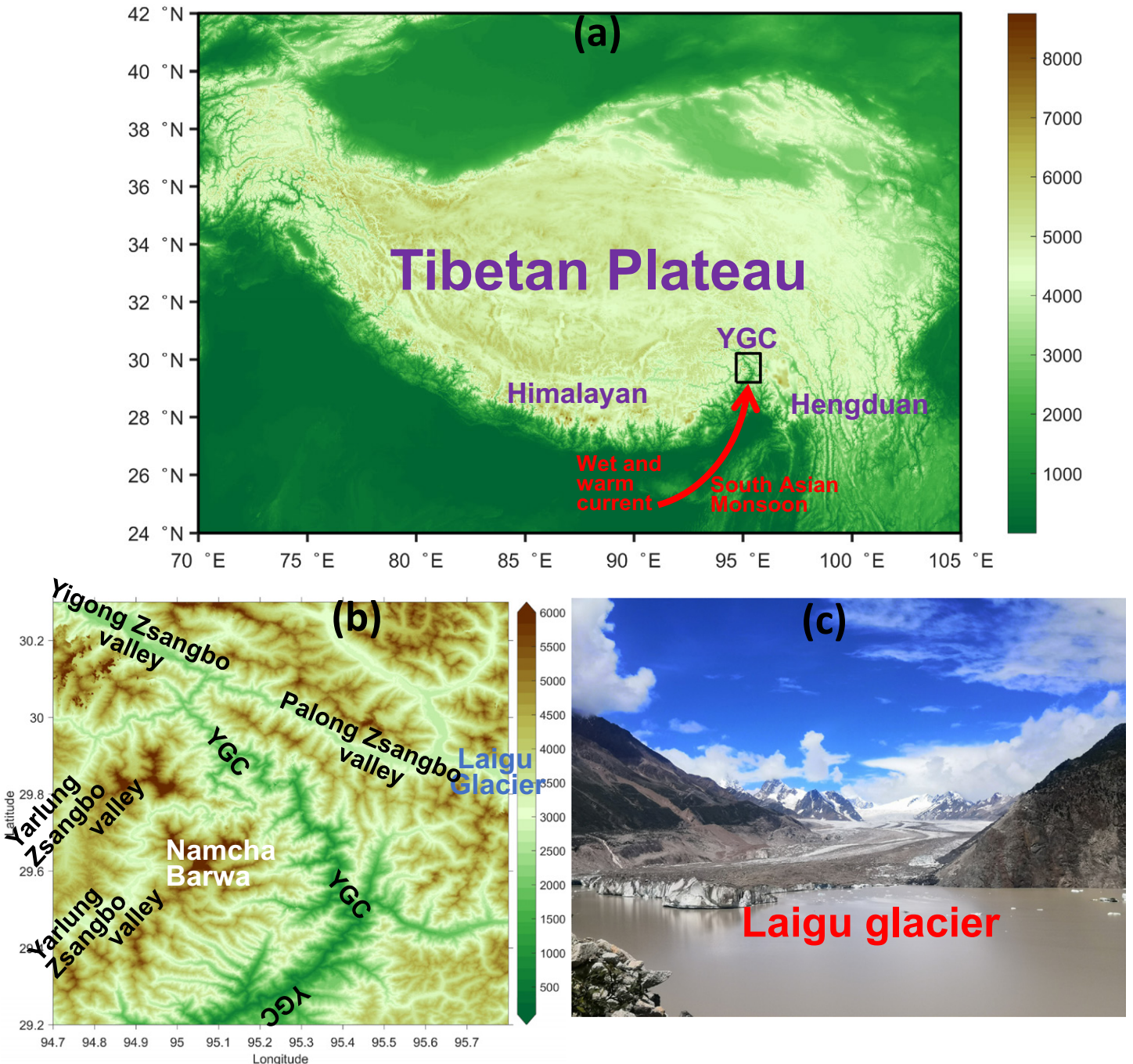


**Fig. 1.** (a) Location of the Yarlung Zsangbo Grand Canyon (YGC). (b) Digital elevation model (DEM) of the YGC region, and (c) photograph of the Laigu Glacier in the YGC region. Photo credit: Xuelong Chen.

of the plateau (Ma et al. 2023, 2008; Zhao et al. 2018). There is a lack of observational data for the YGC region. A comprehensive observation network for water vapor variations, cloud activity, local circulation, and land–air interactions in the YGC can help us to determine the relationship between the water vapor transport in the YGC and heavy precipitation in the SEP and the physical process that determines the precipitation intensity, especially for cases of strong precipitation.

Mountain meteorological conditions vary quickly and are complex. The successful establishment of the Mesoscale Alpine Programme (MAP; Bougeault et al. 2001), the Mountain Terrain Atmospheric Modeling and Observations (MATERHORN) Program (Fernando et al. 2015), and the Innsbruck-Box (i-Box; Rotach et al. 2017) datasets provides us with comprehensive mountain meteorological and mountain boundary layer process observations.

These datasets have strongly supported previous scientific research on mountain land-air interactions and mountain meteorology. However, observations in the TP mountainous environment are scarce. China conducted the first Tibetan Plateau Scientific Expedition and Research Program (FTEP) between the 1970s and the 2010s (1971–2017; Yao 2019). This program achieved a number of scientific results in the YGC region (Gao et al. 1985). It was found that the YGC serves as an important water vapor channel in the TP. However, observations with respect to the time, frequency, and spatial coverage in the YGC region during the FTEP period are limited, and therefore, there are insufficient data to determine the mechanisms controlling the evolution of the weather around the YGC. The Second Tibetan Plateau Scientific Expedition and Research program (STEP), which was launched in August 2017 (Yao 2019), established a scientific research team for the “investigation of precipitation process in the water vapor channel of the Yarlung Zsangbo Grand Canyon” (INVC) in the SEP (see sidebar). The research team designed a monitoring network to fill the observational data gaps in the YGC during the FTEP. A comprehensive system for observing the water vapor, cloud activity, and mountain–atmosphere interactions was constructed in the YGC region. This comprehensive observation experiment in the YGC region also makes it possible to study subtropical mountain meteorology. The developed network was constructed to monitor a comprehensive set of parameters in this area. This paper introduces this initiative in detail.

### **Introduction to the observation system**

Water vapor from the south passes through the YGC and enters the hinterland of the plateau. Observations show that the water vapor transport along the YGC reaches Pailong, and then branches eastward into the Palong Zsangbo valley, northwestward into the Yigong Zsangbo valley, and westward into the upper reaches of the Yarlung Zsangbo valley (Fig. 1b) (Gao 2012). The monitoring network was constructed in these valleys, and it extends along the south lowland area to the north highland area through the YGC to fully characterize the possible links between the water vapor changes and the physical processes of cloud precipitation. The locations of the observation sites are shown in Fig. 2. Table 1 presents information about the equipment at each site. The observation network consists of two cloud radar instruments, two sets of sky-view imagers, two micro rain radar (MRR) instruments, three sets of raindrop disdrometers, eight sets of global positioning system (GPS) water vapor instruments, 19 sets of rain buckets, three sets of microwave radiometers (MWR), three sets of radiosonde, seven sets of eddy covariance instruments, and two sets of automatic weather stations. Table S1 in the supplemental material presents the information about the variables that can be observed by each type of instrument. The construction of the network was completed in 2021, and it will be maintained for the next 3 years.

In the selection of the specific locations of the observation stations, the direction of the water vapor transport was considered and the interference of human activities on the observation signals was minimized. In addition, access to a power supply and the safety of the equipment also influenced the site selection. The water vapor in the YGC is influenced by the South Asian monsoon. The signal of the South Asian monsoon comes from the

### **Yarlung Zsangbo water vapor canyon expedition and research project**

Chinese scientists launch the largest scientific program on the Tibetan Plateau to date in 2017, the Second Tibetan Plateau Scientific Expedition and Research Program (STEP). STEP focuses on water–ecosystem–human activities interaction, the unbalanced Asian Water Tower, and accompanying potential risks. STEP designated 10 major scientific tasks and 19 key research areas. Yarlung Zsangbo Grand Canyon (YGC) is one of the key research areas, due to its special role played in the water cycle of the Asian Water Tower. This paper introduces the progress of scientific activity in the YGC under the umbrella of STEP.

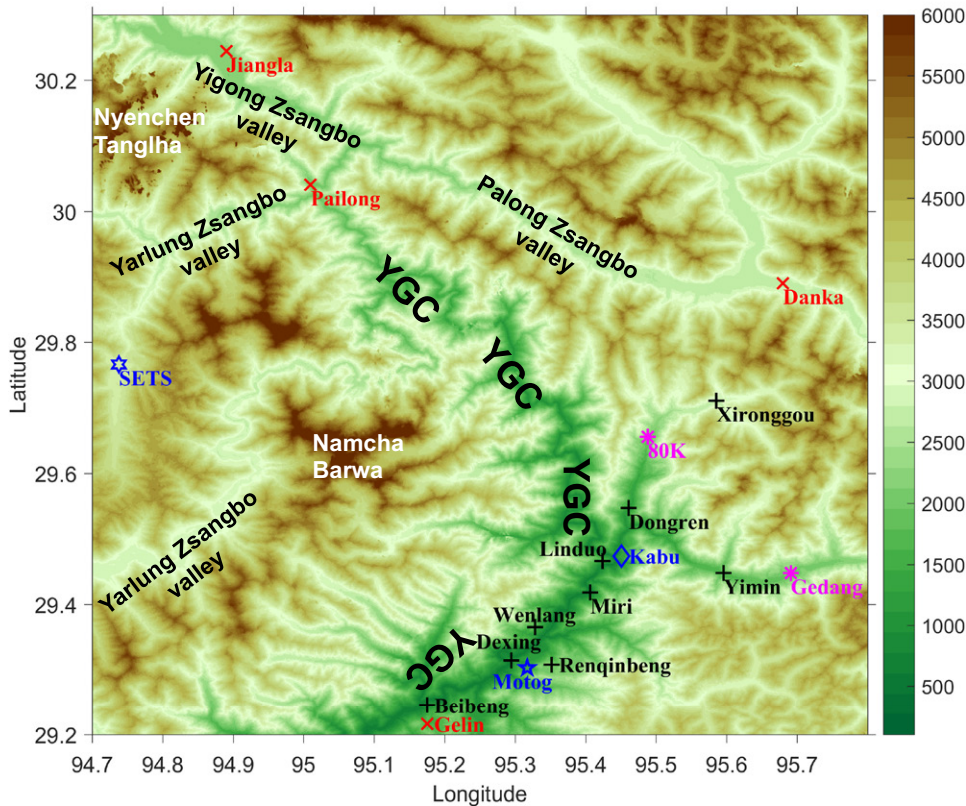


**Fig. 2.** Locations of observation sites and types of instrumentation at the observation sites in the Yarlung Zsangbo Grand Canyon region. The background shows a digital elevation model (DEM) map (unit: m). The black + symbols denote the sites with rain gauges. The red  $\times$  symbols denote the sites with global positioning system (GPS), eddy covariance, and rain gauge instruments. The magenta \* symbols denote the sites with AWS and rain gauge instruments. The blue stars denote the sites with GPS, eddy covariance, laser disdrometer, X- and Ka-band cloud radar, micro rainfall radar, microwave radiometer, radiosonde, all-sky camera, and rain gauge instruments. The blue diamonds denote the sites with GPS, eddy covariance, microwave radiometer, radiosonde, all-sky camera, and rain gauge instruments. The blue hexagrams denote the sites with GPS, eddy covariance, microwave radiometer, radiosonde, all-sky camera, micro rainfall radar, raindrop video disdrometer, and rain gauge instruments.

south of the YGC; therefore, it was important to deploy observation sites in a south–north transect along the YGC. MWRs were used to detect the variations in temperature and humidity at the southern entrance (Motog), midsection (Kabu) of the YGC, and upper reaches of the Yarlung Zsangbo valley (SETS). The MWR at the Motog site was designed to capture the monsoon signal at the entrance. The Kabu site is located in the YGC valley. Its MWR was used to analyze the impacts of local circulation on the water vapor. The SETS site was located in the north–south subbranch of the Yarlung Zsangbo valley in the main body of the TP. The MWR at the SETS site was employed to investigate the heat island over the main body of the TP. The vertical structure of the atmosphere through the YGC region was analyzed using the MWRs at these three sites. Their vertical temperature and humidity profiles combined with ground radiation, and energy balance observations from the eddy covariance system, can be used to study the mechanisms of the water vapor changes in the different valleys.

To improve the accuracy of fine-grid numerical simulations of the YGC area, micrometeorological observation systems were established at different altitudes (1,279–3,330 m). The YGC is also a key area for studying complex mountain meteorological processes within the vicinity of the plateau. Seven sets of eddy covariance stations were installed to observe the land–air water and energy exchanges at the Gelin, Motog, Kabu, Danka, Pailong, Jiangla, and SETS sites, which are located in different valley branches in the YGC region (Fig. 2).

**Table 1.** Equipment employed at each station along the Yarlung Zangbo Grand Canyon (YGC).

No.	Site name	Equipment	Brand	Observation period
1	Xirang (29.039°N, 94.898°E, 511 m)	Automatic weather station	CR1000X, HMP155A, CS106, 034B	Nov 2018–Dec 2019
2	Beibeng (29.245°N, 95.175°E, 865 m)	Rain gauge	Hobo RG3	Nov 2018–present
3	Gelin (29.227°N, 95.175°E, 1,789 m)	Eddy covariance	CSAT3, Licor7500, Kipp and Zonen	Apr 2021–present
		GPS water vapor	Trimble NetR9 GNSS Receiver	Apr 2021–present
		Rain gauge	Hobo RG3	Apr 2020–present
4	Wenlang (29.365°N, 95.338°E, 1,245 m)	Rain gauge	Hobo RG3	Jun 2020–present
5	Dexing (29.324°N, 95.294°E, 737 m)	Rain gauge	Hobo RG3	Jun 2020–present
6	Renqinben (29.307°N, 95.351°E, 2,058 m)	Rain gauge	Hobo RG3	Jun 2020–present
7	Motog (29.312°N, 95.317°E, 1,279 m)	Eddy covariance	CSAT3, Licor7500, Kipp and Zonen	Nov 2018–Apr 2021
		GPS water vapor	Trimble NetR9 GNSS Receiver	Dec 2018–July 2021
		Rain gauge	Hobo RG3	Nov 2018–Apr 2021
		Ka band cloud radar	Sichuang, <a href="https://www.sun-create.com/">https://www.sun-create.com/</a>	Nov 2018/19
		X-band dual-polarization phased-array radar (XPAR)	Naruida, <a href="http://www.naruida.com/">http://www.naruida.com/</a>	October 2019–present
		Micro rain radar	METEK MRR	Jul 2020–present
		Microwave radiometer	Radiometrics MP3000	Dec 2018–Dec 2019
		Three-rotor drone radiosonde	Three-rotor drone + Vaisala RS41-SGP radiosonde	31 Oct–6 Nov 2020
		Cloud cover	EKO ASI-16 Sky imager	Oct 2019–Dec 2021
		Laser disdrometer	PS32, Huatron	Dec 2020–present
8	Miri (29.418°N, 95.406°E, 830 m)	Rain gauge	Hobo RG3	Nov 2018–present
9	Linduo (29.466°N, 95.444°E, 840 m)	Rain gauge	Hobo RG3	Jun 2020–present
10	Yimin (29.448°N, 95.596°E, 1,751 m)	Rain gauge	Hobo RG3	Jun 2020–present
11	Gedang (29.448°N, 95.691°E, 1,953 m)	AWS	CR1000X, HMP155A, CS106, 034B	Jun 2020–present
		GPS water vapor	Trimble NetR9 GNSS Receiver	Jun 2020–present
12	Kabu (29.474°N, 95.451°E, 1,421 m)	Eddy covariance	CSAT3, Licor7500, Kipp and Zonen	Nov 2018–present
		GPS water vapor	Trimble, NetR9 GNSS Receiver	Nov 2018–present
		Rain gauge	Hobo RG3	Nov 2018–present
		Three-rotor drone radiosonde	Quadcopter drone + Vaisala RS41-SGP radiosonde	21–31 Oct 2020
		Microwave radiometer	North Sky Dome, MWP967KV, <a href="http://www.sky-dome.cn">www.sky-dome.cn</a>	Nov 2018–present
13	Dongren (29.547°N, 95.461°E, 1,149 m)	Rain gauge	Hobo RG3	Nov 2018–present
14	80K (29.655°N, 95.488°E, 2,100 m)	AWS	Campbell	Nov 2018–present
15	Xironggou (29.710°N, 95.585°E, 2,750 m)	Rain gauge	Hobo RG3	Nov 2018–present
16	Danka (29.890°N, 95.680°E, 2,709 m)	Eddy covariance	CSAT3, Licor7500, Kipp and Zonen	Nov 2018–present
		GPS water vapor	Trimble, NetR9 GNSS Receiver	Jun 2020–present
		Rain gauge	Hobo RG3	Nov 2018–present
17	Pailong (30.041°N, 95.009°E, 2,081 m)	Eddy covariance	Campbell open-path, Kipp and Zonen	Nov 2018–Mar 2021
		GPS water vapor	Trimble, NetR9 GNSS Receiver	Jun 2020–Mar 2021
		Rain gauge	Hobo RG3	May 2019–Mar 2021

(Continued)

**Table 1. (Continued).**

No.	Site name	Equipment	Brand	Observation period
18	SETS (29.766°N, 94.738°E, 3,326 m)	Eddy covariance	CSAT3, Licor7500, Kipp and Zonen	Nov 2018–present
		GPS water vapor	Trimble NetR9 GNSS Receiver	Jun 2020–present
		Rain gauge	Hobo RG3	Jun 2020–present
		Quadcopter drone radiosonde	Quadcopter drone + Vaisala RS41-SGP radiosonde	13–19 May 2019 27 Jul–2 Aug 2019 13–25 Oct 2019
		Microwave radiometer	North Sky Dome, MWP967KV, <a href="http://www.sky-dome.cn">www.sky-dome.cn</a>	Jun 2020–present
		Two-dimensional raindrop video disdrometer (2DVD)	JR 2D	Nov 2021
		Cloud cover	EKO ASI-16 Sky imager	Nov 2020–present
		Micro rain radar	METEK MRR2	Apr 2021–present
19	Jiangla (30.244°N, 94.890°E, 2,224 m)	Eddy covariance	Campbell open-path, Kipp and Zonen	Jun 2021–present
		GPS water vapor	Trimble NetR9 GNSS Receiver	Jun 2021–present
		Rain gauge	Hobo RG3	Jun 2021–present

Figure S1 in the online supplemental material illustrates the topography in a 1.2 km × 1.2 km area around these sites. The SETS station is located on the floor of a Y-shaped valley. The Jiangla station is located on a 15° slope in the northwest–southeast-oriented Yigong Zsangbo Valley. The Danka station is on a 13° slope in the northwest–southeast-oriented Palong Zsangbo Valley. The Pailong station is located on the floor of a straight segment of the YGC. The valley's axis is inclined from northwest to southeast with a slope of 5°. The Kabu station is located on a small hilly island in the YGC. The Gelin station is located on a 45° slope in the southern part of the YGC river valley. The instruments at the Motog site were installed at the station operated by China Meteorological Administration, which is in the flattest area among the sites. The eddy covariance system collects information about the sensible heat, latent heat, four radiation components, soil temperature and moisture, precipitation, pressure, and wind speed and direction. These sensors can provide information for analysis of the surface energy turbulent fluxes, local circulation, and water vapor in the different valleys. A detailed analysis of the surface energy balance in the different areas of the YGC is helpful to explain the changes in the wind and water vapor in the valley.

The cloud and precipitation observations mainly focused on the vertical structures of the precipitating clouds and the related microphysical processes. The Motog site is considered to be a supersite for cloud precipitation observation instruments and analysis of the relationship between cloud activity and the valley topography. X-band cloud radar and Ka-band cloud radar instruments were employed to detect the vertical structure of the cloud precipitation. MRR, and raindrop spectrometer were employed to obtain data on the phase state of the precipitation particles, the vertical velocity of the air in the clouds, and the raindrop size distribution. GPS water vapor instruments were installed in the southern (Gelin, Motog), central (Kabu), eastern (Gedang), northern (Pailong, Jiangla), northeastern (Danka), and western (SETS, southeast Tibet station of Chinese Academy of Sciences) parts of the YGC to analyze how the water vapor is transmitted northward through the channel. A new rain gauge network was constructed to quantify the spatial and temporal variations in the precipitation in the YGC region. To demonstrate the possibility for investigating the two previously stated scientific issues using these observations, the following section presents some preliminary results based on these instruments.

## Preliminary findings

**Relationship between the water vapor transported along the YGC and extreme precipitation on the SEP.** The precipitation on the SEP may have an important relationship with the water vapor transported along the YGC (Gao et al. 1985; Yuan et al. 2022). Figure 3 shows the temporal variations in the anomalies of specific humidity on 4 days (from day 1 to day 4) before an extreme rainfall event (regional mean daily rainfall rates  $\geq$  the 90% percentile in region I, shown by the white rectangle in Fig. 3f) on the SEP. These time series scenes reveal that abnormally humid air moved from the foot of the Himalayas (around 27°N and 850 hPa in Figs. 3a–e) to the SEP (around 30°N and 500 hPa in Figs. 3a–e). The positive specific humidity distributed above the YGC may provide necessity for the extreme precipitation on the SEP.

To further examine the relationship between the water vapor transport and extreme rainfall, we used the Weather Research and Forecasting (WRF) Model to simulate the water vapor flux during extreme rainfall events in 2019. The general shortcoming of the WRF precipitation simulation nudged with the European Centre for Medium-Range Weather Forecasts' reanalysis dataset version 5 (ERA5; Hersbach et al. 2020) is that it cannot capture strong rainfall period. We tested many WRF parameterization schemes at a 1 km grid resolution. It was found that when an optimized combination of parameterization schemes in WRF can better capture the variations in the wind and water vapor concentration in the YGC channel, the model produced the best simulation results for extreme rainfall in the YGC (Fig. S2). These results were derived from our evaluation of the WRF Model against the surface wind measurements from the eddy covariance instruments

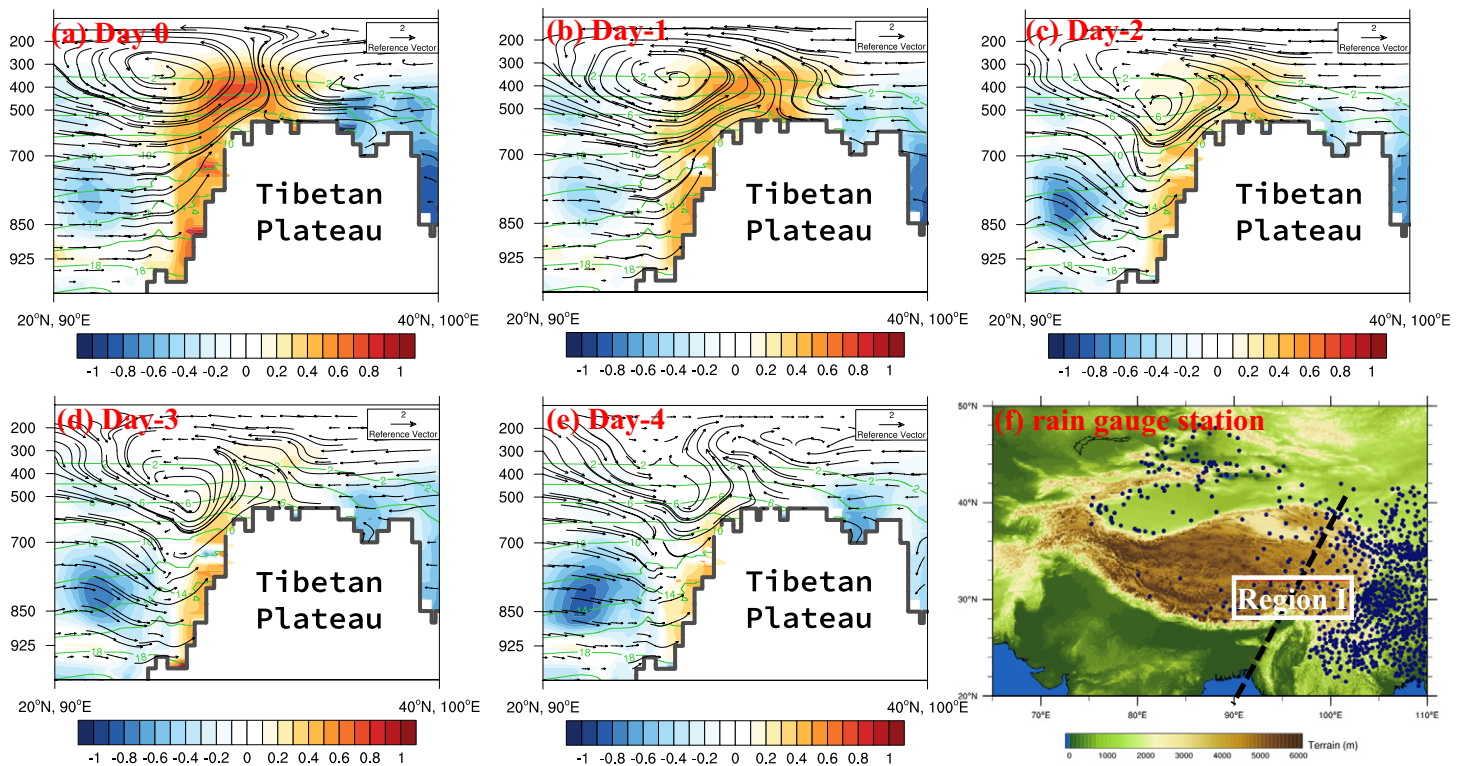


**Fig. 3.** Meridional distribution of anomalies of specific humidity [color-filled contours in (a)–(e)] against the climatology of the specific humidity [green contours in (a)–(e)], and the wind speed (black arrows) during the extreme precipitation periods [regional mean daily rainfall rates  $\geq$  the 90% percentile in region I, shown by the white rectangle in (f)]. The vertical cross section runs from 20°N, 90°E to 40°N, 100°E [black dashed line in (f)], which traveled along the grand valley from south to north. Day 0 denotes the day when the extreme precipitation occurred. Day-1, ..., Day-4 denote 1, ..., 4 days before the extreme precipitation events. The abnormality for Day-1, ..., Day-4 is the difference between the specific humidity and wind speed and the climatology of Day-0. MERRA2 data were used to diagnose the results for the period 1980–2014. The blue points in (f) denote the rain gauge sites operated by the China Meteorological Agency on and around the TP.

installed in the YGC. It is more reasonable to use vertical wind profile measurements to verify the accuracy of the simulated water vapor flux in the YGC. Unfortunately, this remote area has a low aerosol content, so light detection and lidar wind equipment cannot be used in this region.

To capture the water vapor changes in the different parts of the YGC, three MWRs were employed to determine the dynamic changes in the vertical atmospheric temperature and humidity profiles in the canyon. The MWR adopts a radiosonde-based-training artificial neural network algorithm to retrieve the vertical temperature and humidity profiles. To verify the accuracy of the MWR retrievals, a total of 264 rawinsondes were launched. Motog, Kabu, and SETS sites have a collection of 49, 73, and 142 radiosonde data, respectively. The temperature and humidity profiles retrieved from these three MWRs were verified using the radiosonde data (Fig. S3). The results show that the mean biases of the MWRs' temperature data at the Kabu and SETS sites were less than 0.44 K, with root-mean-square errors (RMSEs) of  $\sim$ 3 K. The RMSEs of the specific humidity were less than  $1.74 \text{ g kg}^{-1}$ , and the absolute mean biases were less than  $1 \text{ g kg}^{-1}$  at the three sites. The coefficients of determination for both temperature and humidity are greater than 0.8. The Motog site has a high bias for the retrieved temperature less than 280 K. Motog site has a different MWR instrument than the other two sites. This might be the reason why the site has a different performance. Therefore, the MWR temperature data should be used with caution at this site. We chose one of the strongest rainfall processes in 2021 to demonstrate the benefits of using MWR data to analyze of the relationship between the water vapor and rainfall processes in the YGC (Fig. 4). The intensive rainfall event occurred on 30 June and 3 July 2021, reflected by the four rain gauges. Before this intensive rainfall event, the water vapor column observed by the MWRs at the Motog and Kabu sites increased stably from 24 to 30 June. These observations reveal the importance of water vapor accumulation to the break in heavy rainfall. This observation network can further benefit numerical simulations of the heavy rainfall in this direction.

The elevation of Motog is about 1,279 m and Kabu is around 1,421 m. Motog is at the southern entrance of the YGC, and Kabu is in the midsection of the YGC. Hereby, Motog has a higher TCWV than Kabu, since the moisture in the YGC comes from the south entrance. Kabu has a strong TCWV diurnal variation, with high TCWV in the daytime and relative low values in the night time. This might be because Kabu is more influenced by the daytime upslope and night downslope wind. The daytime upslope comes from the south entrance of YGC, which is more wet than the downslope wind comes from the north mountains. This explains why Kabu has a stronger TCWV variation than that of Motog shown in Fig. 4.

**Potential physical process controlling the precipitation intensity.** The relationships between the atmospheric conditions and precipitation intensity are important for understanding and modeling extreme rainfall. The convective available potential energy (CAPE) and total column water vapor (TCWV) represent the atmospheric conditions, which were observed by the instruments. Figure 5 shows the comparison of the statistical values of the convective energy, TCWV, and cloud-base height during precipitation events at three locations in the YGC region. The SETS site is located on the mainland of the TP, while the Kabu and Motog sites are situated in the valley of the YGC. The TCWV is the lowest at the SETS site compared to the other two sites. This can be explained by the fact that the water vapor transported from the south was released as it ascended along the valley of the YGC. The CAPE at the Motog site did not increase with increasing precipitation intensity, but the TCWV increased with increasing rainfall intensity. This indicates that the TCWV plays a more important role than the CAPE in the heavy precipitation at the Motog site. The cloud-base height of

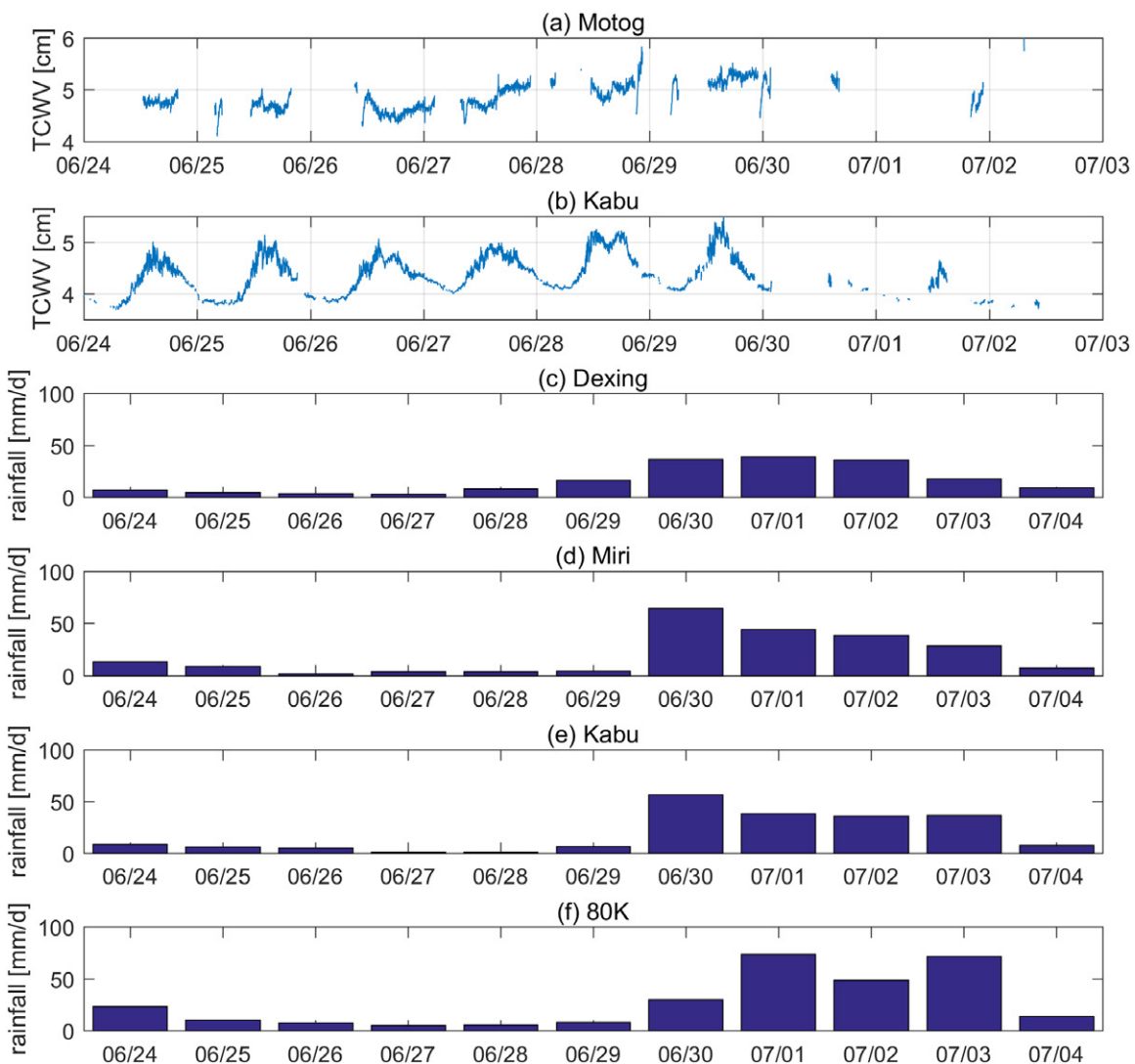


**Fig. 4.** (a),(b) Total column water vapor (TCWV; unit: cm) observed every 2 min at the Motog and Kabu sites, (c)–(f) daily rainfall observed at Dexing, Miri, Kabu, and 80 K from 24 Jun to 4 Jul 2021, during which period the strongest rainfall process in 2021 occurred. The gaps in the TCWV data were caused by power shortages and removal of the interference of the rainfall on the signals of the MWRs.

Motog also changed slightly. For no-rain times, the CAPE at Motog site was much higher than that at the other two sites. We are inclined to conclude that it is not convection that locally produces rainfall at the Motog site. The Kabu and SETS sites had CAPE values close to zero for no-rain periods, while their values increase with rainfall intensity. The TCWV were higher during the precipitation events than during the nonprecipitation periods at the Kabu and SETS site. Both the convective energy and vapor condition played roles in the rainfall at these two sites. The cloud-base height generally decreased with increasing precipitation intensity at the Kabu and SETS sites. These results may indicate that at the Kabu and SETS sites, vertical convection (reflected by the CAPE and the cloud-base height changes) and increased TCWV are important for the occurrence of extreme rainfall events.

**Vertical cloud structure observed by the radar.** The variations in the vertical structures of the clouds observed by the cloud radar at the Motog site are important for analyzing the physical and dynamic processes of the clouds that lead to precipitation. Figure 6 shows a comparative analysis of two cloud types. It shows the reflectivity factor, radial velocity, velocity spectral width, and vertical atmospheric velocity observed by the cloud radar from

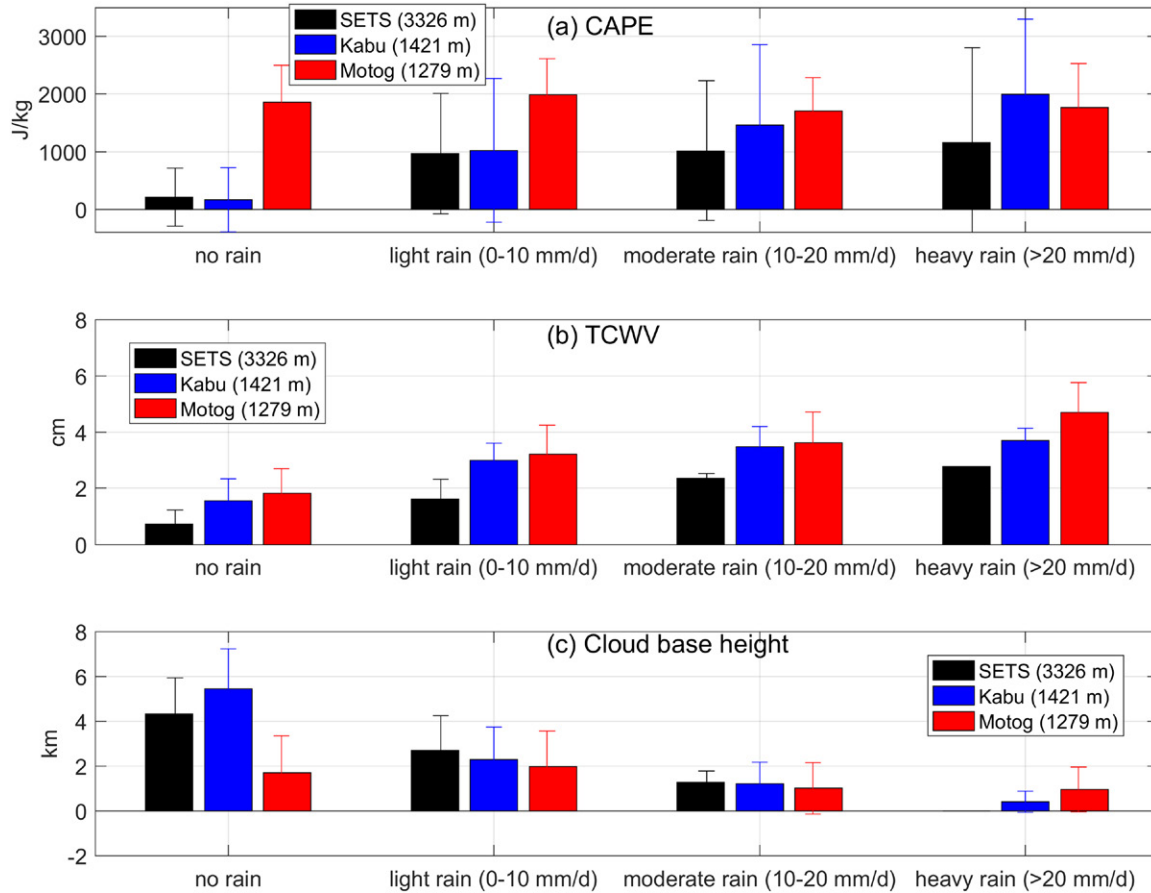


**Fig. 5.** (a) Convective available potential energy (CAPE), (b) total column water vapor (TCWV), and (c) cloud-base height corresponding to different daily rainfall intensity (units:  $\text{mm day}^{-1}$ ); the lengths of the error bars are two standard deviations. The daily averages of the CAPE, cloud-base height, and TCWV were used to conduct the statistical analysis presented in this figure.

2000 Beijing time (BJT) 27 August to 2000 BJT 28 August 2019. The vertical atmospheric velocity was estimated by using the terminal velocity of the smallest particles in reflectivity spectral density data (Gossard et al. 1997; Kollias et al. 2001). The positive (negative) atmospheric velocities denote upward (downward) movement. The altocumulus cloud occurred from 2100 BJT 27 August to 0500 BJT 28 August. The vertical scale of the altocumulus cloud was 6 km (the height ranged from 6 to 12 km above ground level, AGL). The strongest echo reached 19 dBZ (Fig. 6a). The vertical velocity (Fig. 6d) shows that ice particles in the upper part and bottom boundary of the altocumulus clouds moved upward during the initial formation stage of the altocumulus clouds (2100–2300 BJT). A wider spectral width (Fig. 6c) was also noted in the two regions of upward movement, indicating the growth of ice particles during the initial stage. An updraft, evidenced by the estimated positive atmospheric velocity, contributed to the growth of ice particles in the altocumulus clouds. Cumulonimbus precipitation occurred at 1430–2000 BJT 28 August when the cloud top reached a height of 12 km, and the  $0^\circ\text{C}$  brightband layer appeared at about 4 km AGL. The strongest reflectivity factor was 21 dBZ. The ice droplets above the  $0^\circ\text{C}$  brightband layer were characterized by a small radial velocity, while the radial velocity of the liquid particles below the  $0^\circ\text{C}$  brightband layer was large up to  $9 \text{ m s}^{-1}$ . The spectral width increased rapidly when the ice particles passed through the  $0^\circ\text{C}$  brightband layer, indicating a phase transformation from ice to liquid particles. During the early precipitation period (1500–1800 BJT), the atmosphere above the  $0^\circ\text{C}$  brightband layer mostly moved upward. Then, it began to change to downward movement when precipitation occurred. These cloud radar observations provide a view of the physical and dynamic processes involved in cloud

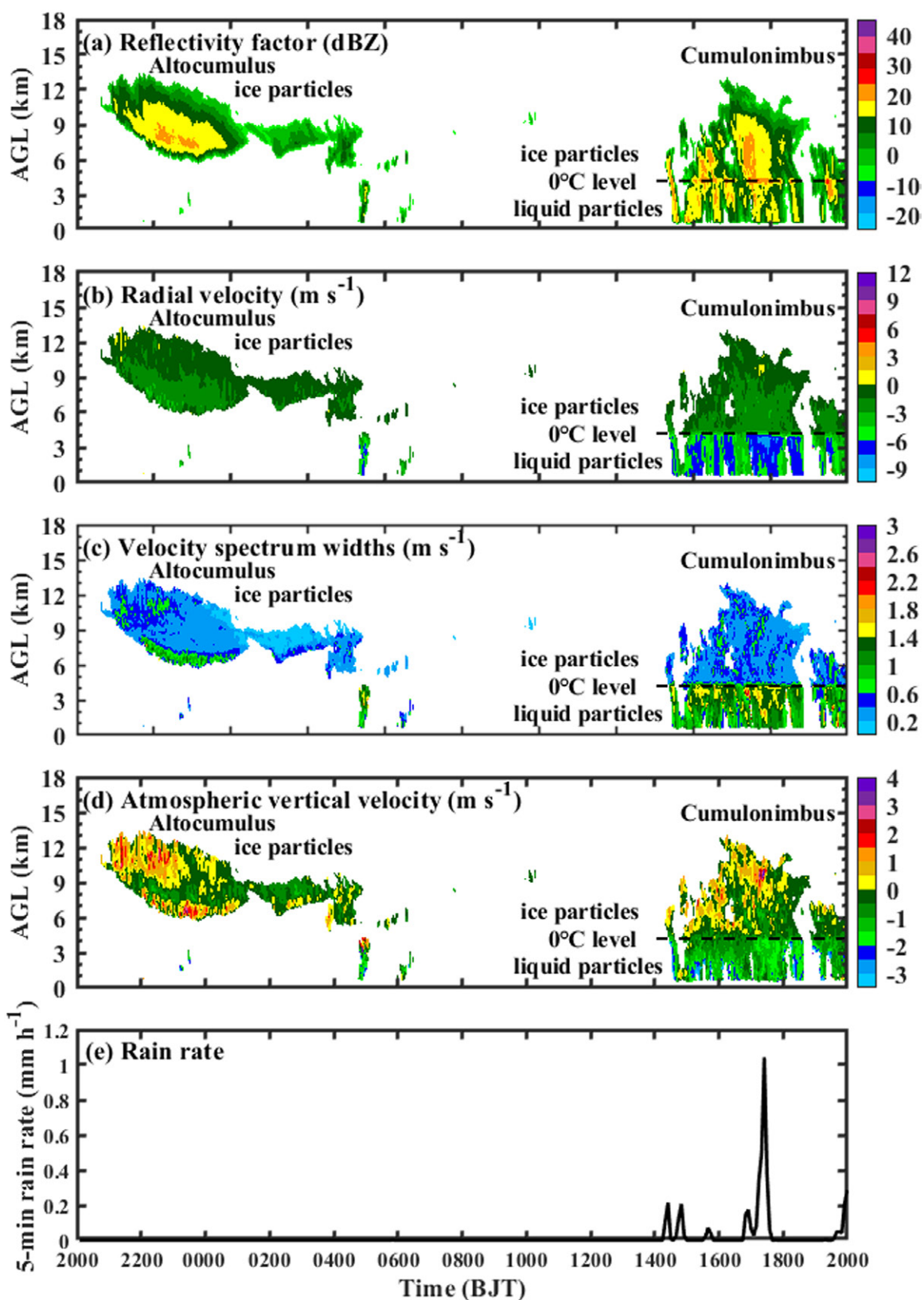


Fig. 6. Variations in the (a) reflectivity factor, (b) radial velocity, (c) velocity spectrum width, (d) atmospheric vertical velocity measured by the Ka cloud radar, and (e) 5-min rain rate with time and height observed by the laser disdrometer at the Motog site between 2000 BJT 27 Aug and 2000 BJT 28 Aug 2019.

and precipitation formation. The cloud radar data can also be further used to diagnose the dynamic process of extreme rainfall events.

Through analysis of 1 year of Ka-band cloud radar data recorded at the Motog site, Zhou et al. (2021) demonstrated that two peaks in the cloud-base height occurred at 0–1 and 2–3 km.

The low clouds at 0–1 km corresponded to precipitating clouds, and the upper-level clouds at 2–3 km is nonprecipitable clouds. Using the rain gauge network data in the YGC, Chen et al. (2023) reported that early morning (around 0400 local time) has the highest precipitation frequency. Cloud radar result from Zhou et al. (2021) shows that clouds tended to form frequently at night. It would be interesting to investigate whether the seeder and feeder mechanisms (Robichaud and Austin 1988) produced by the upper-level and low-level clouds, have caused night heavy rainfall in the YGC.

**Microphysical characteristics of convective and stratiform rainfall.** The raindrop size data can be used to improve the microphysical scheme in weather and climate models. Raindrop spectrum analysis can benefit extreme rainfall prediction and disaster prevention. To investigate the raindrop spectrum, 2D video disdrometer (2DVD) was setup at the SETS site. The raindrop spectrum data obtained from 1 May to 31 September 2022 at the SETS site were used in this study (Fig. 7). The precipitation intensity did not exceed  $25 \text{ mm h}^{-1}$  during this period. The raindrops were divided into five intensity (rainfall rate) categories: (i)  $\leq 0.1$ , (ii)  $0.1\text{--}1$ , (iii)  $1\text{--}5$ , (iv)  $5\text{--}10$ , and (v)  $>10 \text{ mm h}^{-1}$ . All five categories exhibited the highest peaks of particle concentration [ $N(D)$ ] at a diameter of 0.35 mm, which is smaller than the values reported by Steiner and Waldvogel (1987). With increasing raindrop size, the raindrop number concentration decreased. The spectrum width increased with increasing rainfall intensity. The largest contribution to the total precipitation (63.3%) was from the rainfall rate of  $<1\text{--}5 \text{ mm h}^{-1}$ , which accounted for 37.0% of the total precipitation duration. The rainfall rate of  $0.1\text{--}1 \text{ mm h}^{-1}$  contributed 60.2% of the total precipitation duration and 20.7% of the total precipitation. The  $0.2\text{--}2 \text{ mm}$  particle size class contributed 99.5% of the total particle number and the  $0.4\text{--}0.5 \text{ mm}$  particles accounted for the highest percentage (17%) of the particle number.

Convective precipitation has a higher possibility of causing extreme rainfall than stratiform precipitation. It is important to differentiate the characteristics of the two types of precipitation in this region. The method developed by Bringi et al. (2003) was used to classify the convective and stratiform precipitation. The spectrum width of the convective

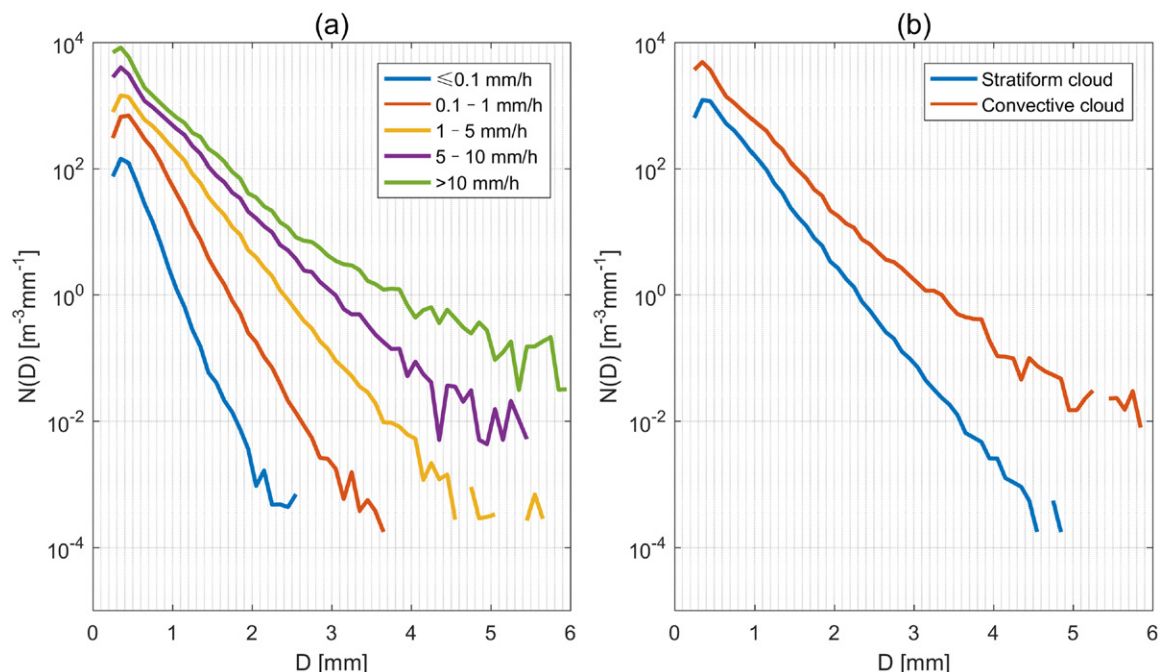


**Fig. 7.** (a) Average raindrop spectrum of five precipitation grades, (b) stratiform and convective precipitation derived from the 2D video disdrometer (2DVD) at the SETS site from 1 May to 31 Sep 2022.  $N(D)$  is the particle concentration.

precipitation was larger than that of the stratiform precipitation (Fig. 7b). The raindrop spectra of the two types of precipitation were characterized by the same peak at 0.35 mm. As the particle diameter increased, the concentration of the convective precipitation was higher than that of the stratiform precipitation. The small- and medium-sized particles dominated the particle concentration. The convective precipitation was characterized by a larger number concentration than the stratiform precipitation. The maximum raindrop diameter for the convective precipitation was 5.75 mm, which was slightly larger than that of the stratiform precipitation (5.25 mm). The spectral variations in the convective and stratiform precipitation at the Motog site (Wang et al. 2021) were similar to what we observed at the SETS site. The Motog and SETS sites are located in the southern and northern parts of the YGC region, respectively. The raindrop spectrum observations at the Motog and SETS sites show that the YGC region has characteristics similar to those of marine convective precipitation. When we compared the raindrop size distribution with Fig. 12 in Dolan et al. (2018), we found that most of the convective rainfall at the SETS site was the collision–coalescence type. This raindrop analysis may provide important clues for determining the mechanisms of raindrop interactions and the formation of heavy rainfall in the YGC region.

We further compare the raindrop spectrum parameters in the YGC with that of lowland area (Xu et al. 2023a,b). Compared with the lowland area, on the SEP, the falling speed of the raindrops was higher, the concentration of the raindrops was smaller, the average raindrop diameter was smaller, and the average  $\log_{10}N_w$  value ( $N_w$  normalized intercept parameter) was larger. The number concentration of the small raindrops for stratiform and convective rainfall was higher on the SEP than in the low-altitude areas. The falling speed of raindrops on the SEP is also higher than that in low-altitude areas. This indicates that the microphysical parameterization scheme of the lowland area may not be applicable to the SEP region.

**A stratiform rainfall event observed by micro rain radar.** Disdrometers provide us with information about the raindrops near the ground after collision, breaking, and aggregation in the atmosphere. An analysis of the raindrops in the atmosphere helps us to understand the formation mechanism of precipitation at the microscale. Figure 8 shows an example of a stratiform precipitation event observed by an MRR at the Motog site on 18 May 2021. The precipitation event on this day mainly occurred between 0400 and 0500 BJT. The precipitation rate measured by a ground rain gauge was  $0.7 \text{ mm h}^{-1}$  during this 1-h period. The reflectivity and falling speed of the precipitation demonstrated that the height of the  $0^\circ\text{C}$  brightband layer was above 3.6 km AGL. Below the brightband layer, the reflectivity factor and liquid water content (LWC) increased with decreasing altitude. The maximum reflectivity factor was 35 dBZ and the LWC was less than  $0.3 \text{ g m}^{-3}$ . When the falling speed was less than  $6 \text{ m s}^{-1}$ , falling speed remained unchanged in height, whereas for falling speeds greater than  $6 \text{ m s}^{-1}$ , it decreased with decreasing height, indicating that the large rain droplets were broken during their fall. Figure 8d shows the changes in the raindrop size distribution with height. The stratiform rainfall drops were dominated by small- and medium-sized particles, with diameters less than 3 mm. The concentration of small raindrops with a diameter of less than 0.5 mm decreased with decreasing height, especially below 2 km AGL, which may have been caused by evaporation. The concentration of raindrops with a diameter of 0.75–3.0 mm increased with decreasing height, which may have been due to the collision of small raindrops and the fragmentation of large raindrops during the falling process.

In the future, raindrop spectrometer data, information on rain droplet growth and breakage from the MRR, and cloud vertical structure and cloud vertical velocity data from the cloud radar system can be used to analyze the micro dynamic processes of the growth and dissipation of heavy rainfall. The aim is to gain a better understanding of the typical atmospheric

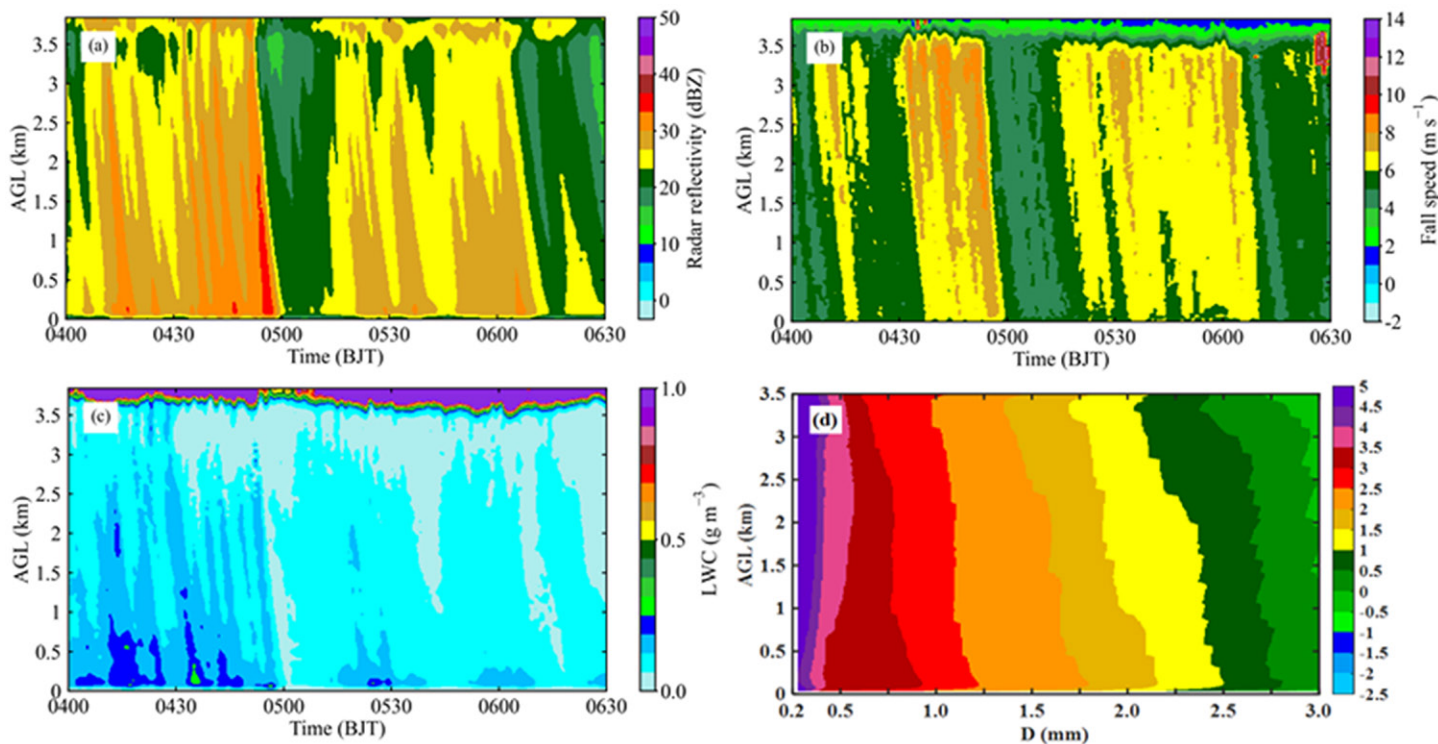


**Fig. 8.** Stratiform rainfall observed by micro rain radar on 18 May 2021 at the Motog site. (a) Reflectivity factor, (b) fall velocity, (c) liquid water content (LWC), and (d) average vertical raindrop size distribution ( $D$ ; unit: mm) profiles. The color bar in (d) indicates the logarithm of the raindrop concentration number.

conditions associated with heavy precipitation and to determine the typical differences between cases of heavy precipitation and weaker events.

### Data storage and management

We have completed the construction of the infrastructure for the monitoring network. The observation network ran smoothly throughout 2021. We have collected the data recorded by the network and have shared the 2018/19 data on the website of National Tibetan Plateau Data Center in China (TPDC; <http://data.tpdc.ac.cn/en/>). More data are expected to be made available in the future after careful data quality checks by other publications (Chen et al. 2023; Xu et al. 2023a,b; Zhou et al. 2021) of the scientific team. The available in situ observations have been used for analysis of the spatial–temporal variations in the rainfall in the YGC, comparison of the raindrop spectrum against low-land areas, and extreme rainfall numerical simulations, which will be published in other journals. The project has entered its full data processing stage. Future relevant data will be processed and provided on the website of the TPDC. The permanent link for downloading the data are <http://data.tpdc.ac.cn/zh-hans/disallow/e68f1de1-3a13-4ae1-90e0-9e3a3f57f912/>.

The datasets produced during this project will be updated annually and released to the scientific community for free 3 years after the end of the experiment, which should aid future research on mountain meteorology.

### Outlook

Debris flows occur constantly in the YGC area during the rainy season. Traffic is blocked yearly due to debris flows. These disasters are closely related to heavy rainfall. Cloud radar, MRR, and MWR instruments were used to obtain the parameters describing the vertical structure of cloud precipitation, the raindrop spectrum, and atmospheric condition. The data analysis revealed the characteristics of the stratiform and convective precipitation in the YGC. MRR and disdrometer systems provide important clues about the growth and

interaction of raindrops for this region. The observation of MWR helps us investigate the atmospheric conditions for different rainfall intensity. We have analyzed the relationship between water vapor and precipitation, the vertical structure of precipitating cloud and nonprecipitating cloud over the SEP using the described observation system. The observation data can further benefit scientists in this direction after sharing the datasets in this paper.

Chen et al. (2023) used the rain gauge data from the INVC project to analyze the precipitation climate in the YGC region. They reported that a clear floor was visible in the afternoon and peak values were exhibited in the early morning. The monthly precipitation in the YGC region shows two peaks in April and July, respectively. The diurnal and monthly variation of precipitation in the YGC are different with main body of the TP. It was also discovered that ERA5 cannot reproduce the diurnal patterns of precipitation in the YGC region. ERA5 showed a wet bias when estimating light cumulus rainfall and a dry bias when estimating heavier (convective) precipitation. The erroneous diurnal variation of ERA5 precipitation (false afternoon rainfall) was due to the CAPE-based convective precipitation scheme. The higher ERA5 precipitation than observed was due to the large-scale rainfall scheme in the Integrated Forecasting System (IFS) of ERA5. These findings indicate that there is still room for improvement of the ERA5 data in the eastern Himalaya region.

The science team of INVC has used the rain gauge network in the YGC to evaluate Integrated Multi-satellitE Retrievals for Global Precipitation Measurement (IMERG; Huffman et al. 2019) precipitation product at subdaily time scales. It was found that IMERG underestimated the total rainfall primarily due to underdetection of rainfall events, with misses being more prevalent than false alarms. It was found that the probability of detection decreased with elevation, leading to increased underestimation of rainfall events at higher elevations, and the false alarm ratio was higher in valley sites. In terms of the hit events, IMERG overestimated the light rainfall events and underestimated the heavy rainfall events and the negative bias in the hit events decreased with elevation. IMERG could capture the early morning peak precipitation in the YGC region but underestimated the amplitude of the diurnal variation. This bias was inherent at the sensor level. This study fills the gap in IMERG validation in a complex mountainous region and has implications for the IMERG algorithm developer to further enhance IMERG accuracy for the mountainous region.

Landslides are predetermined by static factors that can be derived from the surface characteristics and triggered by heavy and prolonged rainfall. Coarse reanalysis and satellite rainfall data are not suitable for studying the extreme rainfall and associated disasters in this region (Chen et al. 2023; Li et al. 2023). Moreover, the Ya'an-Linzhi section of the Sichuan-Tibet railway passes through the YGC region. It is necessary to compile a variety of observation data to reveal the evolution and driving mechanisms of the disastrous weather in this region. The observation network introduced in this paper will provide an observational reference for ecological resilience and disaster prevention.

**Acknowledgments.** This research was funded by the Second Tibetan Plateau Scientific Expedition and Research (STEP) Programme (Grant 2019QZKK0105, 2019QZKK0103) and the National Natural Science Foundation of China (41975009). We thank the three anonymous reviewers and the Editor Dr. Ya-Chien Feng for their kind help to improve the manuscript.

**Data availability statement.** Users can obtain the data through online registration with the TPDC or by contacting the corresponding author directly. The repository digital object identifier (DOI): [10.11888/Atmos.tpdc.271906](https://doi.org/10.11888/Atmos.tpdc.271906).

## References

- Boos, W. R., and Z. M. Kuang, 2010: Dominant control of the South Asian monsoon by orographic insulation versus plateau heating. *Nature*, **463**, 218–222, <https://doi.org/10.1038/nature08707>.
- Bougeault, P., and Coauthors, 2001: The MAP Special Observing Period. *Bull. Amer. Meteor. Soc.*, **82**, 433–462, [https://doi.org/10.1175/1520-0477\(2001\)082<0433:TMSOP>2.3.CO;2](https://doi.org/10.1175/1520-0477(2001)082<0433:TMSOP>2.3.CO;2).
- Bringi, V. N., V. Chandrasekar, J. Hubbert, E. Gorgucci, W. L. Randeu, and M. Schoenhuber, 2003: Raindrop size distribution in different climatic regimes from disdrometer and dual-polarized radar analysis. *J. Atmos. Sci.*, **60**, 354–365, [https://doi.org/10.1175/1520-0469\(2003\)060<0354:RSIDC>2.0.CO;2](https://doi.org/10.1175/1520-0469(2003)060<0354:RSIDC>2.0.CO;2).
- Chen, X., D. Cao, Y. Liu, X. Xu, and Y. Ma, 2023: An observational view of rainfall characteristics and evaluation of ERA5 diurnal cycle in the Yarlung Tsangpo Grand Canyon, China. *Quart. J. Roy. Meteor. Soc.*, **149**, 1459–1472, <https://doi.org/10.1002/qj.4468>.
- , and Coauthors, 2024: Research progress on the water vapor channel within the Yarlung Zangbo Grand Canyon, China. *Atmos. Oceanic Sci. Lett.*, <https://doi.org/10.1016/j.aosl.2024.100462>, in press.
- Dolan, B., B. Fuchs, S. A. Rutledge, E. A. Barnes, and E. J. Thompson, 2018: Primary modes of global drop size distributions. *J. Atmos. Sci.*, **75**, 1453–1476, <https://doi.org/10.1175/JAS-D-17-0242.1>.
- Fernando, H. J. S., and Coauthors, 2015: The MATERHORN: Unraveling the intricacies of mountain weather. *Bull. Amer. Meteor. Soc.*, **96**, 1945–1967, <https://doi.org/10.1175/BAMS-D-13-00131.1>.
- Gao, D. Y., 2012: *Crossing the Yarlung Zangbo Grand Canyon*. Peking University Press, 220 pp.
- , H. Zou, and W. Wang, 1985: Influence of water vapor pass along the Yarlungzangbo River precipitation. *Mt. Res.*, **3**, 239–249.
- Gossard, E. E., J. B. Snider, E. E. Clothiaux, B. Martner, J. S. Gibson, R. A. Kropfli, and A. S. Frisch, 1997: The potential of 8-mm radars for remotely sensing cloud drop size distributions. *J. Atmos. Oceanic Technol.*, **14**, 76–87, [https://doi.org/10.1175/1520-0426\(1997\)014<0076:TPOMRF>2.0.CO;2](https://doi.org/10.1175/1520-0426(1997)014<0076:TPOMRF>2.0.CO;2).
- Hersbach, H., and Coauthors, 2020: The ERA5 global reanalysis. *Quart. J. Roy. Meteor. Soc.*, **146**, 1999–2049, <https://doi.org/10.1002/qj.3803>.
- Huffman, G., and Coauthors, 2019: NASA Global Precipitation Measurement (GPM) Integrated Multi-Satellite Retrievals for GPM (IMERG), NASA. Algorithm Theoretical Basis Doc., version 06, 34 pp., [https://gpm.nasa.gov/sites/default/files/document\\_files/IMERG\\_ATBD\\_V06.pdf](https://gpm.nasa.gov/sites/default/files/document_files/IMERG_ATBD_V06.pdf).
- Jian, J., Z. G. Yang, and G. Zhuo, 2012: Temporal-spatial distributions of severe precipitation event during flood period in Tibet in last 30 years. *Plateau Meteor.*, **31**, 380–386.
- Kollias, P., B. A. Albrecht, R. Lhermitte, and A. Savtchenko, 2001: Radar observations of updrafts, downdrafts, and turbulence in fair-weather cumuli. *J. Atmos. Sci.*, **58**, 1750–1766, [https://doi.org/10.1175/1520-0469\(2001\)058<1750:ROOUDA>2.0.CO;2](https://doi.org/10.1175/1520-0469(2001)058<1750:ROOUDA>2.0.CO;2).
- Kukulies, J., D. Chen, and M. Wang, 2020: Temporal and spatial variations of convection, clouds and precipitation over the Tibetan Plateau from recent satellite observations. Part II: Precipitation climatology derived from global precipitation measurement mission. *Int. J. Climatol.*, **40**, 4858–4875, <https://doi.org/10.1002/joc.6493>.
- Li, L., X. Chen, Y. Ma, W. Zhao, H. Zuo, Y. Liu, D. Cao, and X. Xu, 2023: Implications for validation of IMERG satellite precipitation in a complex mountainous region. *Remote Sens.*, **15**, 4380, <https://doi.org/10.3390/rs15184380>.
- Lin, C., D. Chen, K. Yang, and T. Ou, 2018: Impact of model resolution on simulating the water vapor transport through the central Himalayas: Implication for models' wet bias over the Tibetan Plateau. *Climate Dyn.*, **51**, 3195–3207, <https://doi.org/10.1007/s00382-018-4074-x>.
- Ma, Y., S. C. Kang, L. P. Zhu, B. Q. Xu, L. D. Tian, and T. D. Yao, 2008: Tibetan observation and research platform: Atmosphere–land interaction over a heterogeneous landscape. *Bull. Amer. Meteor. Soc.*, **89**, 1487–1492, <https://doi.org/10.1175/2008BAMS2545.1>.
- , and Coauthors, 2023: Comprehensive study of energy and water exchange over the Tibetan Plateau: A review and perspective: From GAME/Tibet and CAMP/Tibet to TORP, TPEORP, and TPEITORP. *Earth-Sci. Rev.*, **237**, 104312, <https://doi.org/10.1016/j.earscirev.2023.104312>.
- Robichaud, A. J., and G. L. Austin, 1988: On the modelling of warm orographic rain by the seeder-feeder mechanism. *Quart. J. Roy. Meteor. Soc.*, **114**, 967–988, <https://doi.org/10.1002/qj.49711448207>.
- Rotach, M. W., and Coauthors, 2017: Investigating exchange processes over complex topography: The Innsbruck Box (i-Box). *Bull. Amer. Meteor. Soc.*, **98**, 787–805, <https://doi.org/10.1175/BAMS-D-15-00246.1>.
- Steiner, M., and A. Waldvogel, 1987: Peaks in raindrop size distributions. *J. Atmos. Sci.*, **44**, 3127–3133, [https://doi.org/10.1175/1520-0469\(1987\)044<3127:PIRSD>2.0.CO;2](https://doi.org/10.1175/1520-0469(1987)044<3127:PIRSD>2.0.CO;2).
- Wang, G. L., R. R. Zhou, S. Zha Xi, and L. P. Liu, 2021: Comprehensive observations and preliminary statistical analysis of cloud and precipitation in Motuo of Tibet Plateau. *Acta Meteor. Sin.*, **79**, 841–852, <https://doi.org/10.11676/qxb2021.054>.
- Wu, G. X., and Y. S. Zhang, 1999: Thermal and mechanical forcing of the Tibetan Plateau and Asian monsoon onset Part II: Timing of the onset. *Sci. Atmos. Sin.*, **23**, 52–62.
- Xu, X., X. Chen, D. Cao, Y. Liu, L. Li, and Y. Ma, 2023a: Comparisons of rainfall microphysical characteristics between the southeastern Tibetan Plateau and low-altitude areas. *J. Appl. Meteor. Climatol.*, **62**, 1591–1609, <https://doi.org/10.1175/JAMC-D-23-0046.1>.
- , —, X. Zhao, D. Cao, Y. Liu, L. Li, and Y. Ma, 2023b: Microphysical characteristics of snowfall on the southeastern Tibetan Plateau. *J. Geophys. Res. Atmos.*, **128**, e2023JD038760, <https://doi.org/10.1029/2023JD038760>.
- Xu, X. D., C. G. Lu, X. H. Shi, and S. T. Gao, 2008: World water tower: An atmospheric perspective. *Geophys. Res. Lett.*, **35**, L20815, <https://doi.org/10.1029/2008GL035867>.
- Xu, X. M., 2019: Evaluation on order degree of ecological tourist economic system of Brahmaputra Grand Canyon National Park. *Areal Res. Dev.*, **38**, 106–109, 122.
- Yang, W., T. Yao, B. Xu, L. Ma, Z. Wang, and M. Wan, 2010: Characteristics of recent temperate glacier fluctuations in the Parlung Zangbo River basin, southeast Tibetan Plateau. *Chin. Sci. Bull.*, **55**, 2097–2102, <https://doi.org/10.1007/s11434-010-3214-4>.
- Yao, T. D., 2019: Tackling on environmental changes in Tibetan Plateau with focus on water, ecosystem and adaptation. *Sci. Bull.*, **64**, 417, <https://doi.org/10.1016/j.scib.2019.03.033>.
- , and Coauthors, 2012: Different glacier status with atmospheric circulations in Tibetan Plateau and surroundings. *Nat. Climate Change*, **2**, 663–667, <https://doi.org/10.1038/nclimate1580>.
- Yuan, X., K. Yang, H. Lu, Y. Wang, and X. Ma, 2022: Impacts of moisture transport through and over the Yarlung Tsangpo Grand Canyon on precipitation in the eastern Tibetan Plateau. *Atmos. Res.*, **282**, 106533, <https://doi.org/10.1016/j.atmosres.2022.106533>.
- Zhao, P., and Coauthors, 2018: The third atmospheric scientific experiment for understanding the Earth–atmosphere coupled system over the Tibetan Plateau and its effects. *Bull. Amer. Meteor. Soc.*, **99**, 757–776, <https://doi.org/10.1175/BAMS-D-16-0050.1>.
- Zhou, R., G. Wang, and S. Zhaxi, 2021: Cloud vertical structure measurements from a ground-based cloud radar over the southeastern Tibetan Plateau. *Atmos. Res.*, **258**, 105629, <https://doi.org/10.1016/j.atmosres.2021.105629>.